RIJKSUNIVERSITEIT GRONINGEN

BACHELOR THESIS

Measuring the Effect of Atmospheric Dispersion on MICADO Using ScopeSIM

rijksuniversiteit
groningen

Author:
F. R. M. Reid

Supervisors:
J. A. van den Born
Dr. J. Noel-Storr

F. R. M. Reid

Abstract

With increasingly large Earth based telescopes being built, the effect of atmospheric dispersion on telescopes needs to be reevaluated. MICADO aims to be a diffraction limited imager on the ELT and so will be especially sensitive to atmospheric dispersion. It will reverse atmospheric dispersion using an atmospheric dispersion corrector (ADC) by calculating the expected atmospheric dispersion from a model. Differences in models are small but may be significant in the context of MICADO. Spectroscopy is often used to measure atmospheric dispersion on-sky as it shifts the spectral trace spatially as a function of wavelength, making it easy to measure the dispersion. We use ScopeSIM to simulate the output of MICADO's spectroscopy mode with no ADC to see if dispersion was measurable. We then compare the dispersion to that calculated by existing models. In our comparisons, differences of up to 1.64 milli arc seconds were present, significant in the context of MICADO.

Contents

1   Introduction

Observations done by ground based telescopes are affected by atmospheric dispersion at non-zero zenith angles due to the wavelength dependence of the refractive index of air. This elongates the point spread function, leading to distortions in the image (Filippenko, 1982; van den Born & Jellema, 2020). For smaller telescopes, the effect has generally been negligible or, if it needed to be accounted for, models used to calculate dispersion were accurate enough. As the next generation of telescopes start to be built, however, atmospheric dispersion becomes an issue that needs to be reassessed.

Although these telescopes are not yet operational, we can use simulated images to determine how much of an effect we expect dispersion to have on these telescopes. In this report we look at the Extremely Large Telescope (ELT) and specifically at one of its first generation instruments, the Multi-Adaptive Optics Camera for Deep Observations (MICADO) (Davies et al., 2018). MI-CADO aims to be diffraction limited and so will be sensitive to atmospheric dispersion if it is not accounted for properly. We use ScopeSIM (Leschinski et al., 2020) to perform the simulations, which is the official simulator for MICADO.

We use spectroscopy for our analysis as dispersion manifests itself as a function of wavelength in spectroscopic images, shifting the trace spatially. By simulating spectroscopic images at a range of zenith angles we can firstly determine if dispersion is measurable using MICADO and, if so, compute the expected atmospheric dispersion MICADO will see with no corrections and compare this to other models. This gives an idea of the residual dispersion we might expect to see when MICADO is operational.

A more detailed overview of the ELT and MICADO is given in Section 2. Then, a mathematical description of atmospheric dispersion is given, including the atmospheric and refractive index models we use, as well as a description of how dispersion affects spectroscopy in particular in Section 3. In Section 4 we outline the process we use to calculate dispersion using ScopeSIM. Our results and how they compare to other models are shown in Section 5. We then discuss future observations that could be done as well as improvements that could be implemented to improve future analyses done using our method in Section 6. Our conclusions are then given in Section 7.

2   The ELT

Astronomers' ongoing quest for knowledge of our universe has historically driven us to build ever larger telescopes so that we might probe our universe in more detail. Exoplanet and high redshift observations in particular are a major goal of the current astronomical community. Extremely Large Telescopes (ELTs) aim to be the next generation of telescopes to carry on this legacy and achieve these goals.

Telescopes such as the Thirty Meter Telescope (TMT), the Giant Magellan Telescope (GMT), and the ELT will make use of their high resolutions and light gathering capabilities to perform observations that will provide deep insight into exoplanets (Beuzit et al., 2019; Maire et al., 2021) and the formation of our universe (Brandl et al., 2021; Davies et al., 2018; Thatte et al., 2021). However, with the unprecedented size of ELTs, factors that didn't previously need to be considered or were known to some degree of accuracy now must be considered in greater detail. Such factors include atmospheric turbulence and atmospheric dispersion.

Adaptive optics are instrumental in minimising the effects of these factors. For the ELT, single conjugate adaptive optics (SCAO) will be employed in the form of a deformable and tip-tilt mirror (Vernet et al., 2019, 2020). These systems are designed to account for wind, vibrations due to the motion of the ELT, and also to counter atmospheric turbulence. Atmospheric turbulence is measured by wavefront sensors using a bright guide star near the object being observed. Bright guide stars are not always available so modern systems also rely on artificial guide stars produced by lasers. The ELT will use eight of these lasers around the target object being observed. Correction for atmospheric dispersion will be dependent on the instrument.

In order to take full advantage of the new capabilities offered by the ELT, it has been designed to use multiple instruments and to be able to switch between these instruments in minutes. The first generation of instruments are planned to be the Mid-infrared ELT Imager and Spectrograph (METIS) (Brandl et al., 2021), the High Angular Resolution Monolithic Optical and Near-infrared Integral field spectrograph (HARMONI) (Thatte et al., 2021), and MICADO (Davies et al., 2018).

Additional adaptive optics systems can also be integrated to work in conjunction with the instruments. The Multi-Conjugate Adaptive Optics RelaY (MAORY) system will work together with MICADO to take full advantage of the capabilities of the ELT (Ciliegi et al., 2020). MAORY offers an SCAO mode for narrow field-of-view (FOV) observations ($19''$x$19''$) using a bright natural guide star and a multi-conjugate adaptive optics (MCAO) mode which uses three natural guide stars as well as six artificial guide stars to provide corrections over a wider FOV ($50.5''$x$50.5''$) (Ciliegi et al., 2020; Davies et al., 2018). The narrow FOV will have a plate scale of 1.5 mas pixel^{-1} while the wider FOV's plate scale will be 4 mas pixel^{-1}.

2.1   MICADO

MICADO is designed to be diffraction limited, so it will be especially susceptible to effects previously considered negligible or where models were assumed sufficiently accurate. This also makes it a prime candidate for analysing in detail the effects of atmospheric dispersion. MICADO will employ an atmospheric dispersion corrector (ADC) to minimise dispersion but its operation will be based on a model for both the refractive index and geometry of the atmosphere. The differences in current models used to calculate atmospheric dispersion are generally small (Spanò,
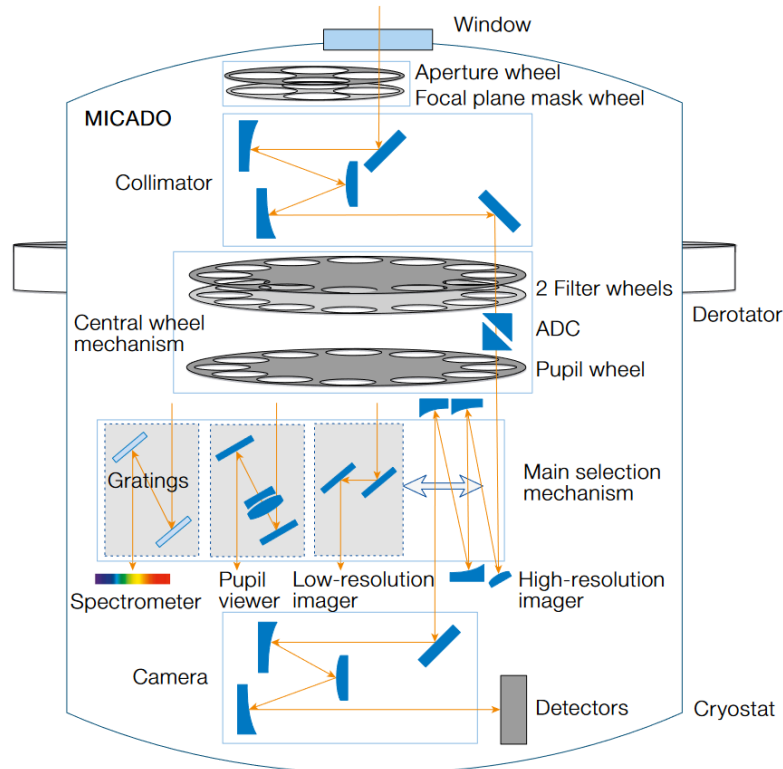
Figure 1: A schematic overview of MICADO. The light from the ELT comes in through the window. A combination of the filter wheels, pupil wheel and main selection mechanism allows the choice of imaging mode and wavelength range. The entire setup is contained within the cryostat. Figure from Davies et al. (2021).

2014) but these differences start to become significant for the precision required by MICADO and the ELT as a whole (Skemer et al., 2009; Wehbe et al., 2020).

MICADO itself will primarily be an imaging instrument that will also be capable of spectroscopy operating in the near infrared (0.8-2.4μm). It will offer four main modes of observation: standard imaging, astrometric imaging, high contrast imaging, and the aforementioned spectroscopy mode. A schematic overview of MICADO can be seen in Figure 1. Some of the key components are discussed below.

Two large filter wheels enable MICADO to hold over 30 filters at any time. This enables MICADO to be flexible with little external intervention. However, the requirements for the filters will make them expensive to manufacture and so it may be that a smaller number of filters will be available initially and the remaining slots are filled over time (Davies et al., 2018).

The ADC is a key component in allowing MICADO to operate to its full potential. This is especially true for the astrometric imaging mode given its sensitivity to differences in radial velocity measurements (van den Born & Jellema, 2020; Wehbe et al., 2019). It uses two counter-rotating Amici prisms in order to reverse atmospheric dispersion, minimising the effect it has on observations. The ADC reverses atmospheric dispersion based on a model. However, this could lead to dispersion being present due to differences between the used model and the dispersion present in reality.

Our analysis of atmospheric dispersion is done using MICADO's spectroscopy mode. Its relevance is discussed further in Section 4. Therefore, we discuss the design of the spectrometer in some detail here. A slit is placed in the focal plane mask using the corresponding wheel to produce a quasi 1D image. Then a filter is selected for the wanted wavelength range. These are a 1.45-2.45 μm filter (HK-band), a 1.15-1.35 μm filter (J-band) or a 0.83-1.45 μm filter (IzJ-band). The HK- and J-band filters are designed to work with a 15″ slit while the IzJ-band filter will use a 3″ length slit. The expected spectral resolution is R$\sim$20000 for a point source and R$\sim$10000 when integrated over the slit. The spectroscopy mode uses the wider FOV and so the lower resolution plate scale.

In order to separate the incoming light into a spectrum, MICADO employs two gratings. These are moved into the light path by the main selection mechanism. One is a cross-dispersing grating which then directs the light onto an Echelle grating, separating the light into the spectrum which is spread over the detectors. Such a setup is optimised for high spectral orders, allowing more detail to be resolved within the spectrum (Baranne et al., 1996; Tull et al., 1995).
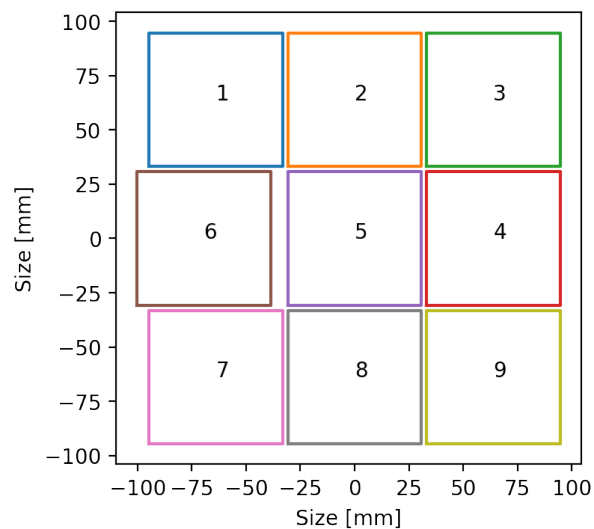
Figure 2: The physical layout of MICADO's nine detectors. Note that detector 6 is shifted to the left slightly compared to the other detectors.

For the detectors, MICADO will use nine H4RG detectors in a 3x3 configuration (Davies et al., 2021). Due to the positioning of the detectors, the cooling requirements, and the location of the detector cables, detector 6 is shifted on the 3x3 grid compared to the other detectors. This can be seen in Figure 2. Another artifact of the detector layout, especially in spectroscopy mode, is that some of the incoming light is lost inbetween the detectors due to the physical limitations of the detectors. When MICADO is operational, this will be handled by using slits at shifted positions so spectral ranges of interest are not lost (Davies et al., 2018).

This detector layout, combined with the cross-dispersed Echelle gratings, leads to a spectral trace over the detectors. This trace starts on detector 1 at the longest wavelength, goes down through detectors 6 and 7. It then restarts at the top of detector 2 and carries on down to detector 5 and 8 where the shortest wavelengths fall on the detector. This trace is specific to the HK-filter as other filters produce different trace layouts over the detectors, but the general

idea for them is similar i.e. starting on detector 1 and so on.
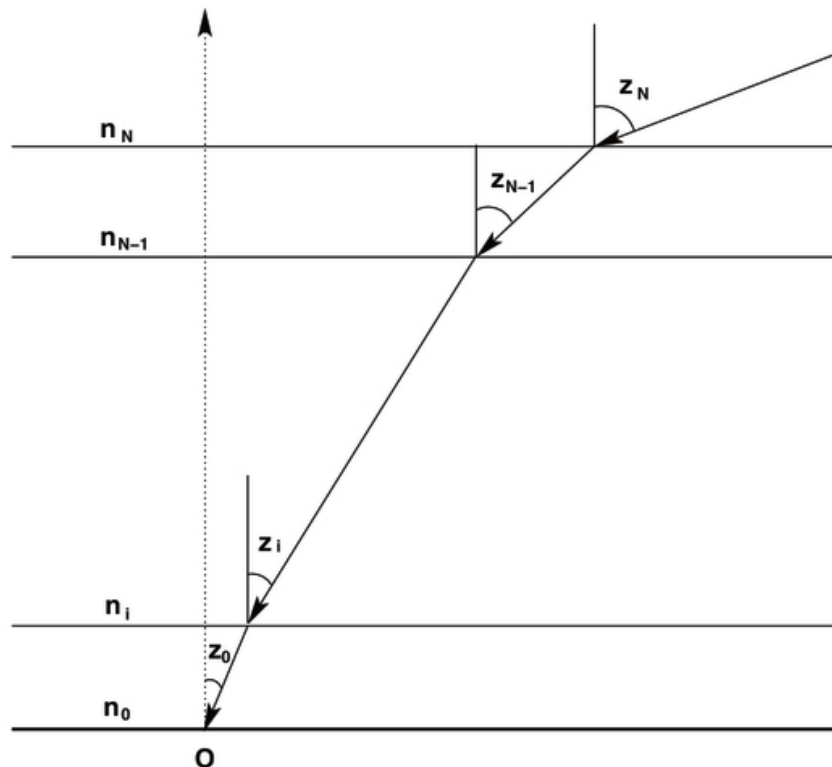
3   Atmospheric Dispersion

3.1   Atmospheric Model

Atmospheric dispersion is the difference in refraction angle between two wavelengths of light that have passed through the atmosphere (Devaney et al., 2008). When light enters the atmosphere it is refracted due to the difference in index of refraction between the vacuum of space and the atmosphere. This refraction follows Snell's law:

$$n_1 \sin \theta_I = n_2 \sin \theta_R \tag{1}$$

where θ_I is the angle of incidence, θ_R is the angle of refraction, n_1 is the index of refraction of the first medium (e.g. space) and n_2 is the index of refraction of the second medium (e.g. the atmosphere).

However, the index of refraction is wavelength dependent meaning that, as light enters the atmosphere at non-zero angles of incidence, shorter wavelengths are refracted more than longer wavelengths, elongating the point spread function observed and distorting the image (Filippenko, 1982; van den Born & Jellema, 2020). There are no analytical models for the wavelength dependence of refractive indices but empirical models are used to calculate these changes. The change in refractive index due to the wavelength one calculates depends on the model chosen.

Figure 3: A diagram showing a multi-layered plane parallel atmosphere and the propagation of a light ray through it. Figure from (Mangum & Wallace, 2015).

Dispersion is also dependant on the geometry of the atmosphere. The choice of atmospheric model has some effect on the calculated dispersion, but for most models it is negligible (van den Born & Jellema, 2020). In our analysis, we consider a plane-parallel model. Such a model assumes a flat geometry for the atmosphere where each layer is parallel to those below it as seen

in Figure 3. The plane-parallel model remains reasonably accurate for small to moderate zenith angles and is simple to derive. Repeated application of Snell's law, Equation 1, leads to the relation:

$$n_0 \sin z_0 = n_N \sin z_N = \sin z_N \tag{2}$$

Here, n_0 is the index of refraction at the observer, z_0 is the angle between the incoming light and the zenith at the observer, n_N is the index of refraction of space (a vacuum) and z_N is the actual zenith angle of the incoming light. We make use of the fact that n_N is 1 to simplify. The refraction, R, is then the difference between z_0 and z_N:

$$R = z_N - z_0 \tag{3}$$

Putting this into Equation 2 and applying the trigonometric identity for the sine of a sum of angles gives:

$$\begin{aligned}
n_0 \sin z_0 &= \sin(R + z_0) \\
&= \sin R \cos z_0 + \cos R \sin z_0
\end{aligned} \tag{4}$$

Note that $R << 1$ and so we can approximate this relation using $\sin R \approx R$ and $\cos R \approx 1$:

$$\begin{aligned}
n_0 \sin z_0 &\approx R \cos z_0 + \sin z_0 \\
R &\approx (n_0 - 1) \tan z_0
\end{aligned} \tag{5}$$

Dispersion is then the difference in refraction between two wavelengths and so can be defined as:

$$\begin{aligned}
\Delta R &= R(\lambda) - R(\lambda_{\text{ref}}) \\
&= (n(\lambda) - n(\lambda_{\text{ref}})) \times \tan z_0
\end{aligned} \tag{6}$$

where λ_{ref} is the index of refraction at a chosen reference wavelength.

More complex models that treat the atmosphere spherically are often used, such as a radially symmetric atmosphere (Mangum & Wallace, 2015) or Cassini's refraction model (Young, 2006), but these will not be treated in this paper.
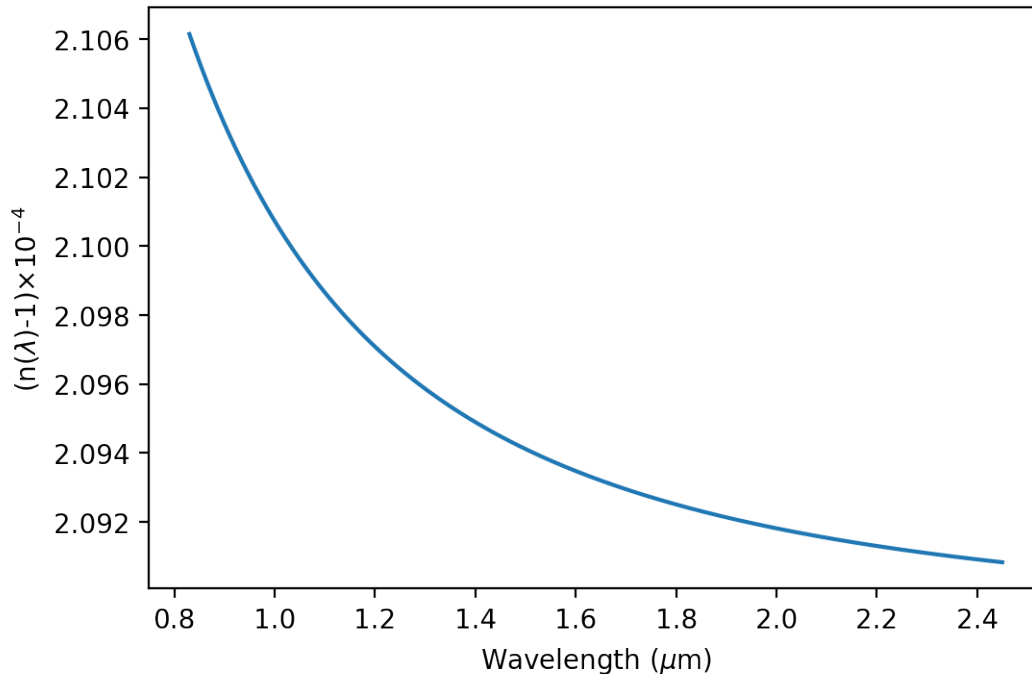
3.2   Index of Refraction

In order to model the refractive index of air, many models are available e.g. Filippenko (1982), Ciddor (1996), Mathar (2007). The choice of model depends on the wavelength, temperature, pressure, and humidity range of interest. For instance, Mathar (2007) is optimised for infrared and longer wavelengths by accounting for resonances that affect the refractive index caused by OH and H_2O. Such models also allow for the CO_2 content of the air to be given. A comparison of various models can be found in Spanò (2014).

From the comparison between models in Spanò (2014), differences in the refractive index are typically of the order of 10^{-8} which can result in differences in dispersion calculations of up to 40 mas in the worst cases for the relevant wavelength range for MICADO. This is a significant amount for MICADO, which has a residual dispersion budget for the ADC of 0.4 mas (van den Born & Jellema, 2020).

The typical value for the refractive index of air is 1.00029 for standard atmospheric conditions and in the optical regime. Variations in the refractive index over the wavelength range of

MICADO are on the order of 10^{-6} as shown in Figure 4. The refractive index will also vary with temperature and pressure changes on the order of 10^{-5} for typical atmospheric values. Humidity has a smaller effect, with variations on the order of 10^{-6} between 0% and 100% humidity. CO_2 content has a much smaller effect on the refractive index, with variations being only 10^{-8}.

Figure 4: The refractive index of air over MICADO's wavelength range. Over the entire range we see a variation of around 2×10^{-6}. Changes in atmospheric conditions also effect the refractive index but the magnitude of this effect is dependent on the parameter.

For modelling the index of refraction, the data we collected uses constant temperature, pressure, CO2 content, and humidity values, so a simple model is used for our analysis; a two term Cauchy equation. This models the refractive index as:

$$n(\lambda) = A + \frac{B}{\lambda^2} \tag{7}$$

3.3   Airmass

In some analyses of atmospheric dispersion, airmass is used instead of the zenith angle, such as Skemer et al. (2009). Converting between the two values can be easily done using the following equation:

$$\text{AM} = \frac{1}{\cos z} \tag{8}$$

where AM is the airmass and z is the zenith angle. This relation comes from the plane parallel model.

3.4   Atmospheric Dispersion in Spectroscopy

Generally, it is preferred to align the slit used for spectroscopy along the parallactic angle. This leads to the atmospheric dispersion occurring along the direction of the slit (Bahrami

& Goncharov, 2011; Wynne & Worswick, 1986). As a result, the dispersion affects the trace purely spatially so that, as you move away from the reference wavelength on the trace, the trace becomes increasingly dispersed at non-zero zenith angles. This setup is also optimised for the function of the ADC to correct the dispersion. For our simulated observations, we aligned the slit with the parallactic angle.

3.5   Expected Dispersion

We can get a preliminary idea of the dispersion we should expect to see in our results. We used the Ciddor model to find the maximum dispersion at each zenith angle we intend to get data for over our wavelength range of interest, 1.5-2.08 μm. This indicated that we would expect close to 5 milli arc seconds (mas) of dispersion at a 5° zenith angle while dispersion would be 91 mas for a zenith angle of 60°. The expected maximum dispersion for our range of zenith angles can be seen in Figure 5. Given MICADO will have a plate scale of 4 mas pixel^{-1} in spectroscopy mode, we expect to be able to detect dispersion using MICADO, especially at larger zenith angles.
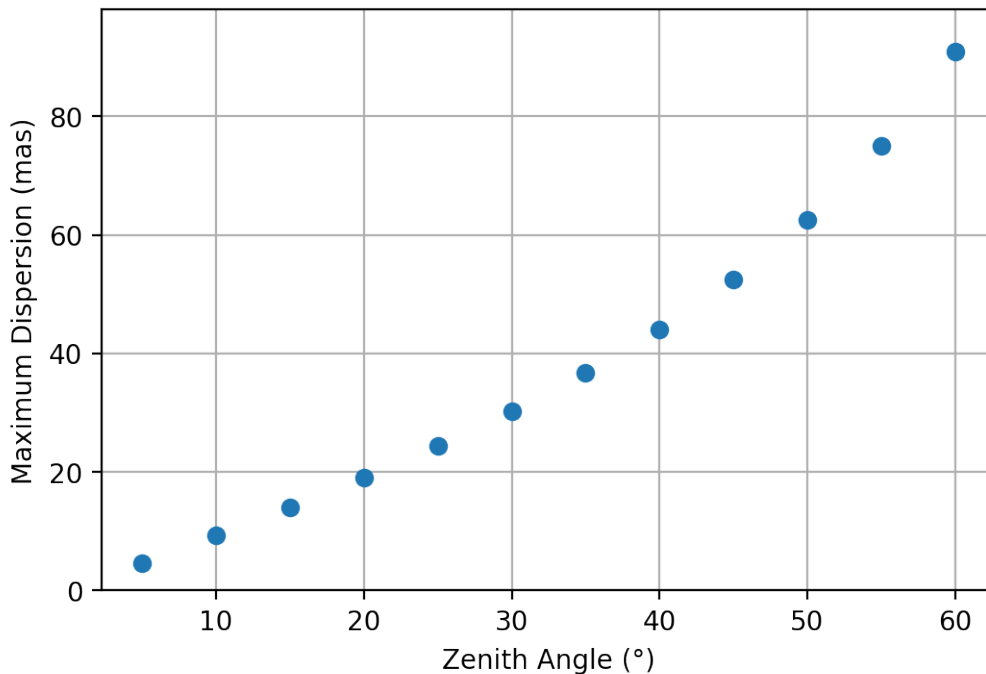
Figure 5: The maximum dispersion we expect to see for our zenith angles of interest. These values were calculated using the Ciddor model and a plane-parallel atmospheric geometry.

4 Method

Direct measurements of atmospheric dispersion from spectroscopic observations have been done previously by Skemer et al. (2009) and Wehbe et al. (2020). Skemer et al. (2009) employed a method whereby the centroid at each wavelength was found by fitting a Moffat profile, allowing the amplitude, centroid, FWHM, and Moffat index to vary. The centroid position is then compared at different zenith angles for a given wavelength to measure the dispersion. This is done for all wavelengths to find the dispersion over the measured range.

Wehbe et al. (2020) used a similar method, although fitting a Gaussian to find the centroid, but looked at multiple spectral orders for each wavelength.

For our analysis, a method similar to Skemer et al. (2009) was used. However, the function used to find the centroid in our analysis was an airy pattern. This was chosen due to the diffraction limited nature of MICADO. Since both methods are only interested in the centroid position, the choice of a different function to find the centroid will not effect the results other than being better suited for their respective instruments.

For our analysis, and for both Skemer et al. (2009) and Wehbe et al. (2020), spectroscopy was used to measure atmospheric dispersion. Spectroscopy is ideal for this as it allows analysis of all wavelengths of interest from a single observation. Additionally, it removes the influence of any change in atmospheric conditions that might vary between observations. Perhaps most importantly, however, any spatial shift at a given wavelength can easily be measured due to the 1d nature of the spatial data resulting from spectroscopy. This makes spectroscopy preferable over imaging for measuring dispersion.

4.1 ScopeSIM

In order to obtain the desired results, we used the python package ScopeSIM (Leschinski et al., 2020) to simulate the output we would expect to see from MICADO when it is operational. More specifically, we use the simulated spectroscopy mode of MICADO to properly analyse the effect of dispersion at different zenith angles.

ScopeSIM is capable of adding or removing multiple effects to the final image it produces. For instance, various types of noise, such as readout noise, can be turned on or off as needed. Atmospheric dispersion is similarly included in such a way by defining the effect and then including it to be applied to the image by ScopeSIM. It should be noted that the current version of ScopeSIM (version 0.5.0 as of writing) does not support the inclusion of atmospheric dispersion and so an older version was used for this research (version 0.1.4). ScopeSIM uses its own model for the refractive index and atmosphere to implement dispersion. Upon inspection of the source code this appears to be the refractive index model of Owens (1967) and a two term odd power expansion of $\tan z$ to model the geometry of the atmosphere.

While atmospheric dispersion was included for our analysis, noise effects previously mentioned were disabled to simplify data analysis. Similarly, atmospheric transmission and absorption lines were disabled as they also interfered with data analysis. In principle, such effects will be mostly eliminated from the final images produced by MICADO in reality anyway so this is not expected to affect the results we obtained in any major way.
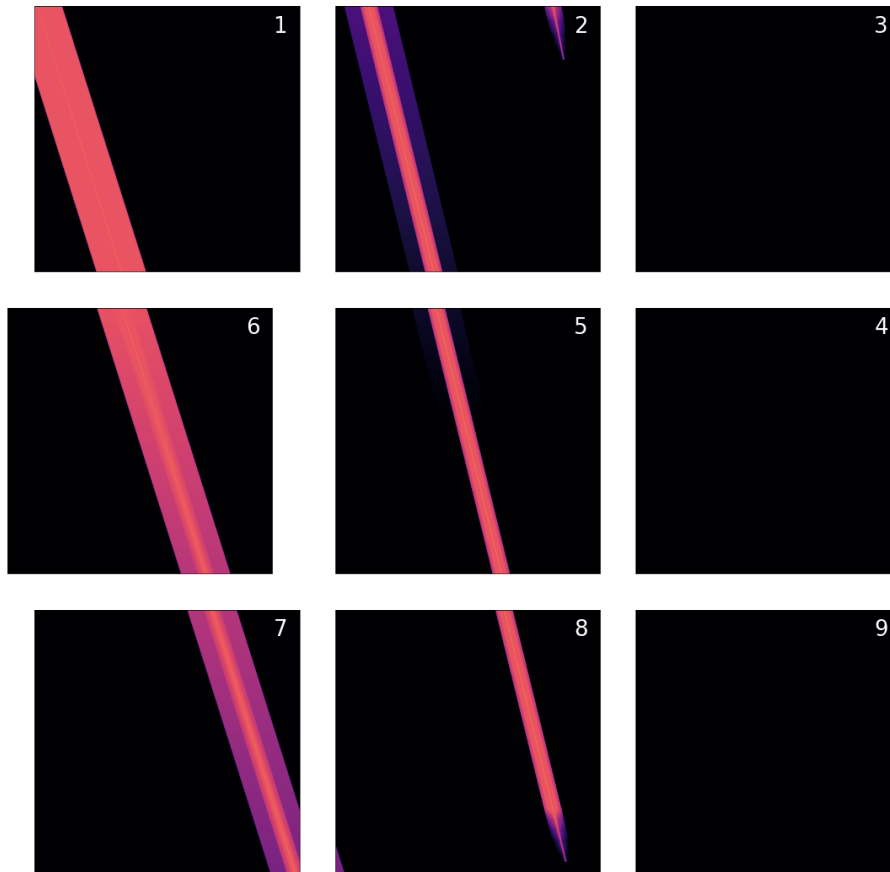
Figure 6: An example of the output given by ScopeSIM from a spectroscopic simulation of a point source. The detector numbers are given in the top right of each detector output. Detector 6 has been shifted as seen in Figure 2. The wider trace seen on detectors 1, 6 and 7 come from thermal bleed due to room temperature black body emission. No trace is present on the rightmost detectors for the HK spectroscopy filter.

The final image produced by ScopeSIM is nine arrays, one for each detector, of 4096x4096 pixels, designed to imitate the image produced by the MICADO optical train. This can then be saved to a fits file and worked with as usual. An example of this output for the spectroscopic mode of MICADO can be seen in Figure 6.
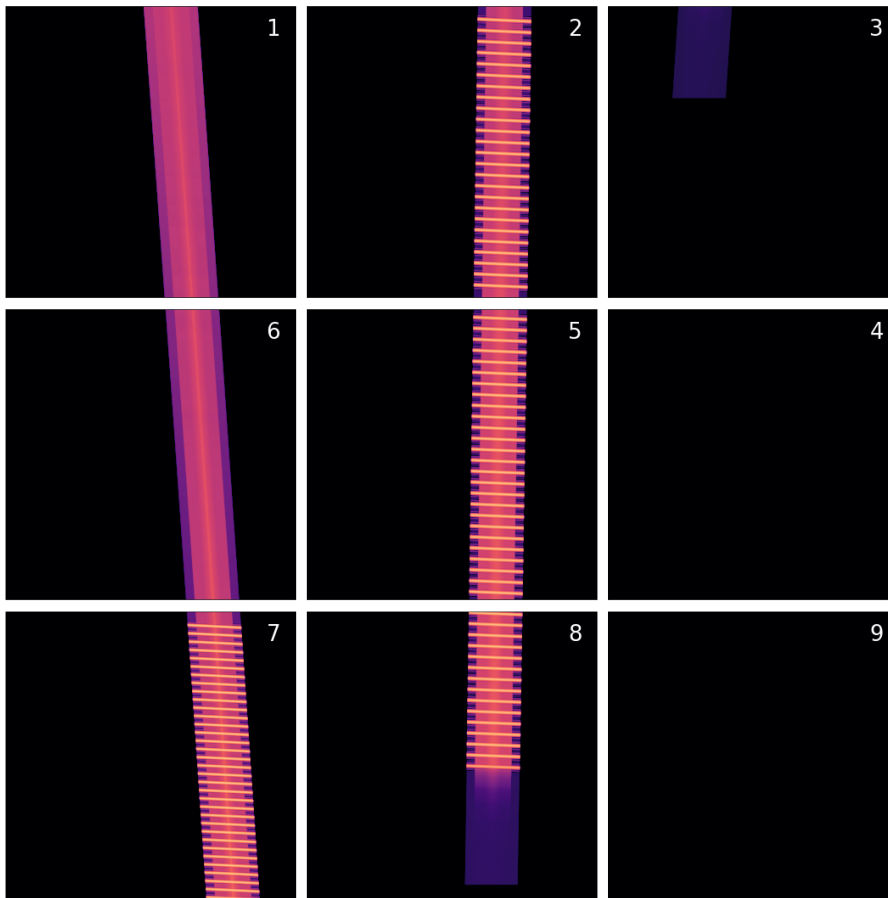
4.2   Calibration

One issue with simulating the spectroscopy mode output with ScopeSIM is that it does not provide any information on wavelength calibration. Typically, calibration is done using continuum and line emission lamps, Fabry-Perot etalon spectra and filters, optical simulations of the instrument or a combination thereof (Abbott et al., 1996; Birkmann et al., 2011; Labiano et al., 2021). Further calibration is often done once the spectrometer is operational using sources with known spectra.

In our case, since we are in a simulated environment, we can define many artificial sources to be "observed" that are only present at specific wavelengths. We were able to calibrate four of the six detectors used by the HK spectroscopy filter, namely detectors 2, 5, 7, and 8, which

encompasses the wavelengths we wish to look at, 1.5-2.08μm. This method could, however, be used for all the detectors when using ScopeSIM.

Using the SynPHOT python package (Lim & Hanley, 2016), sharp spectral peaks were inserted into the source observed by ScopeSIM. Since these are user defined, the wavelength of them is known. We can then match these peaks in the ScopeSIM output to the known wavelengths to find a series of pixel rows that correspond to the defined wavelengths. The calibration frame we generated in ScopeSIM using this process can be seen in Figure 7. Using these data points, a linear fit can easily be applied to determine where on the detector a given wavelength corresponds, even to a subpixel level. While the fit is linear on each detector, it should be noted the relation of pixel row to wavelength is not consistent across all detectors. The calibration results are discussed in Appendix B.

Figure 7: The detector output resulting from the calibration process. The regular peaks come from the chosen artificial sources. No sources were added to detectors 1 and 6 as they were outside the range of interest.

4.3   Measuring Dispersion

Once the calibration frame is generated and we have the calibration results, the images needed to measure dispersion can be generated. For our analysis, we chose a point source to observe. The spectrum used was that of an M2V star taken from Pickles (1998). We also used the
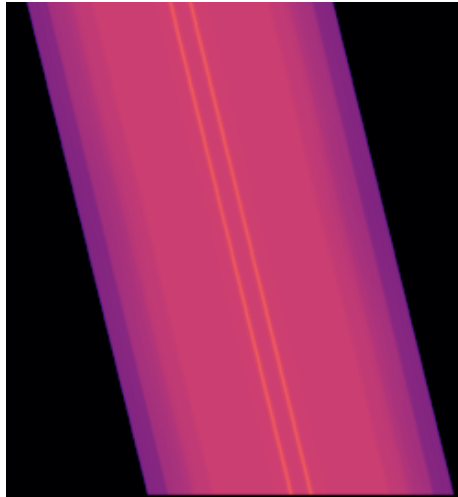
Figure 8: A close-up of the ScopeSIM output of two simulations, one with and one without dispersion, which have been overlaid. The two spectral traces can be seen as the right one has been shifted due to dispersion (60° zenith angle) while the left trace has not been shifted.

HK filter that covers the wavelength range from 1.45 μm to 2.5 μm and the $3000''$ length slit. This encompasses the range that will be used by the low resolution, high FOV imager on MICADO (Davies et al., 2018). It should be noted that the HK filter is in fact designed to work with the longer 15000" slit. However, since our observations were of a point source, and the slit length is only relevant for the spatial data, changing the slit is not expected to change the results.

Since the atmopsheric dispersion included by ScopeSIM depends on the atmospheric conditions given, these must also be defined. In our case, ScopeSIM includes details on typical values found at the Armazones location where the ELT will be located. These are given in Appendix A.

With these parameters chosen, we generate 13 images with zenith angles ranging from 0 to 60 degrees in steps of 5 degrees. Figure 8 shows two of these images overlaid, one at 0° and one at 60° zenith angles. A set of wavelengths are then chosen to measure the dispersion at and the corresponding pixel row is found using our calibration results. We then take the spatial slice on this row and fit a 1D airy pattern point spread function (PSF) to it.

This fit is then used to find the centroid at sub-pixel levels. By comparing the location of the centroid at the selected wavelengths against the centroid location for the image at a zenith angle of 0 degrees, the dispersion in pixels is found. This is then converted to mas using the plate scale of the detector, 4 mas pixel^{-1}.

Once we have measured the dispersion at each wavelength, we then use our chosen model for the refractive index, Equation 7, and the dispersion given by the plane parallel model, Equation 6, to produce our own model for the refractive index based on our data. This is then directly compared with other refractive index models.

4.4   Extracting the Spectrum

The simulated output given by ScopeSIM of MICADO's spectroscopy mode gives the full detector array, meaning the spectral trace is not isolated to a single image but spread over the nine detectors. In order to extract this spectral trace, further data processing must be done. The method we employed is rudimentary but works well when observing only one source or a set of sources with a particularly bright member.

By making use of the NumPy package `argmax` function (Harris et al., 2020), the brightest pixel in each row on each detector was located. Extracting the trace then simply involves taking the desired number of pixels either side of this peak. Using a point source centered in the observing slit, the spatial width of the peak is roughly 20 pixels meaning the full spatial slice of the spectral trace is unnecessary.

5 Results

5.1 Spatial Fitting

When finding the centroid, a linear least-squares fit of an airy pattern is done to the 1d spatial slice of the detector output at a given wavelength. This is undertaken using the `curve_fit` function from the SciPy python package (Virtanen et al., 2020). An example of such a fit can be seen in Figure 9. The `curve_fit` function also gives the error in the centroid position. The mean error in the centroid positions is ± 0.02 pixels or ± 0.09 mas with the maximum error being ± 0.03 pixels or ± 0.1 mas.
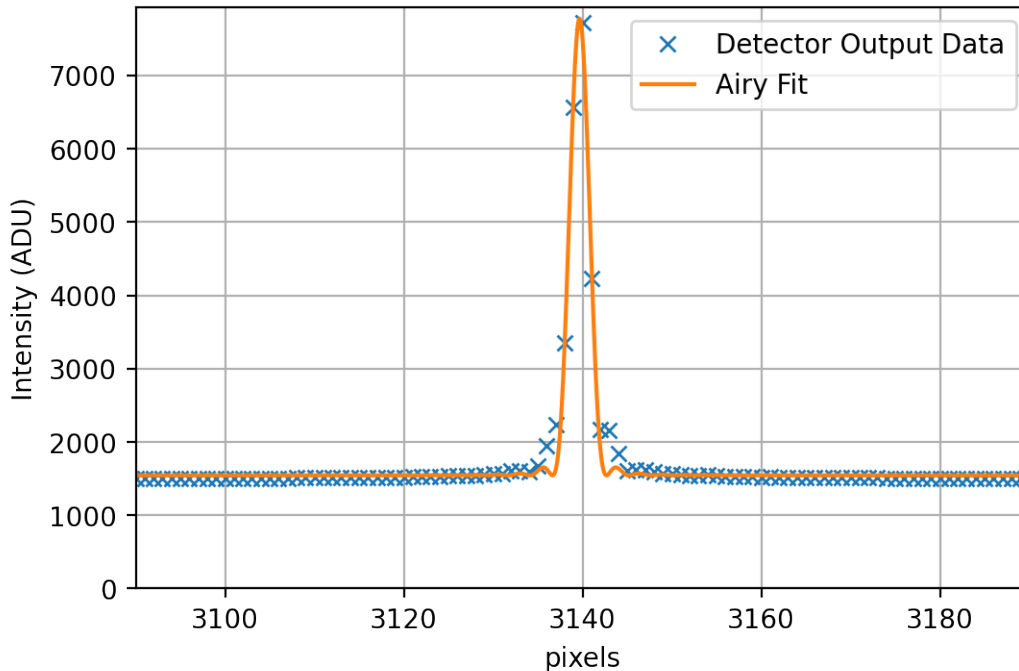

Figure 9: An example of the spatial fitting done to find the centroid. Such a fit is done across all 13 images at each wavelength of interest. The fit gives the centroid location and the error in this location.

5.2 Dispersion Data

Using the methods outlined in Section 4, the final dispersion data was obtained. From this data, we also obtained our best fit Cauchy coefficients. These were then used to model the dispersion we would expect across the spectrum observed by MICADO. We also compared our model to the Ciddor (Ciddor, 1996) and Mathar (Mathar, 2007) models using the AstroAtmosphere python package (van den Born & Jellema, 2020) in the following sections. In all cases, the plane parallel model was used for the atmospheric geometry.

From our data best fit, we obtained the Cauchy coefficients $A = 1.000208 \pm 0.000001$ and $B = (1.1800 \pm 0.0002) \times 10^{-6}$. Figure 10 shows the data and our best fit model overlaid, although limited to zenith angles in steps of $10°$ for legibility. A complete set of graphs can be found in Appendix C. One feature of interest is the step nature of the dispersion data obtained from ScopeSIM. While the airy pattern fit can obtain the centroid at sub-pixel levels, unless the

17
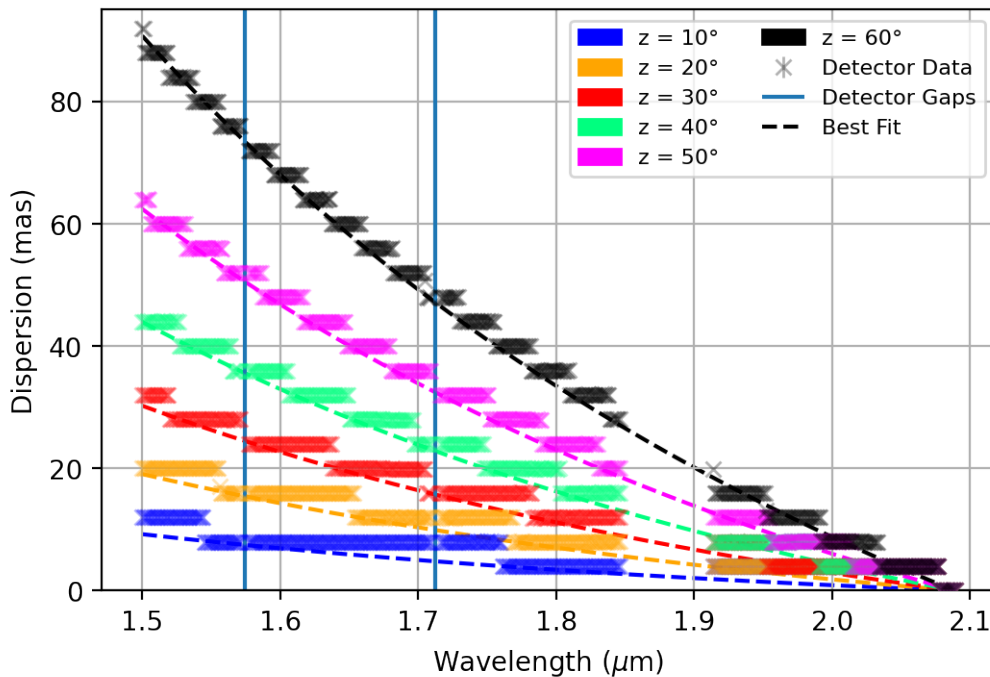
Figure 10: The dispersion data obtained from analysing the ScopeSIM output with the best fit of this data. The colours denote the zenith angle for the data/model. The smaller detector gaps between detectors 2, 5, and 8 are marked by vertical lines. The large gap in detector data around 1.9 μm is the gap from the trace going from detector 2 to detector 7.

dispersion is enough to shift the centroid by a full pixel (or 4 mas), it will appear to have the same dispersion as the pixels either side of it.

Another noticeable feature of Figure 10 are the gaps in the detector data. The gaps between detectors 2 and 5, and 5 and 8 have been marked while the gap between detectors 2 and 7 can be seen around 1.9 μm.
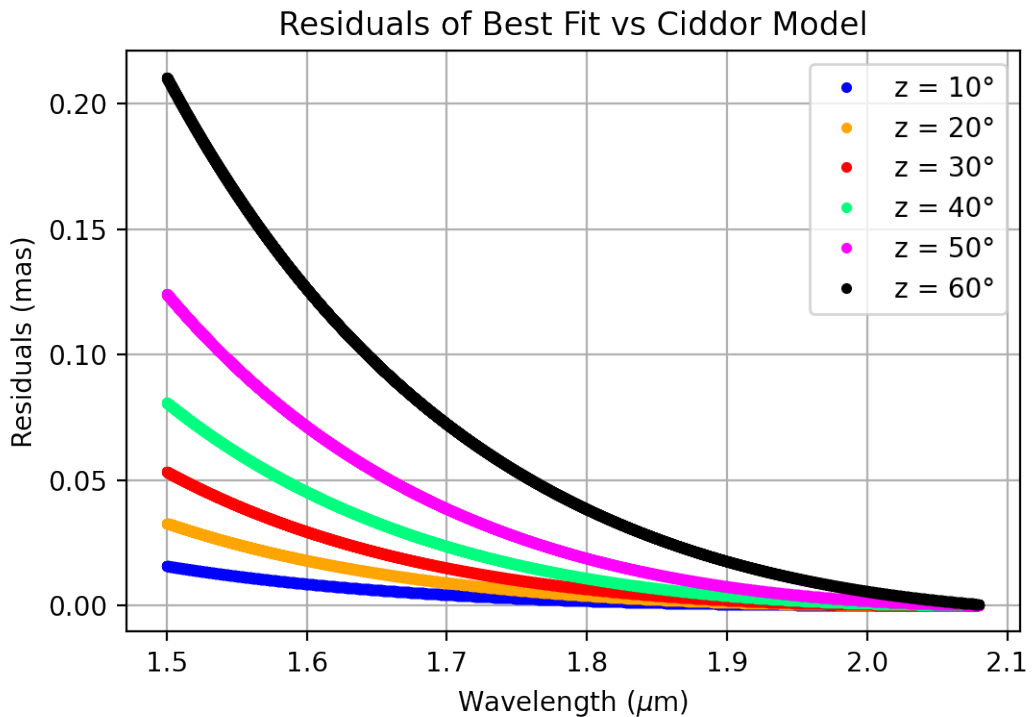
5.3   Comparison to the Ciddor Model

With our data and best fit giving us our model for dispersion, we then compare this to the dispersion predicted by the Ciddor model. Our comparison in Figure 11 shows that our model is in good agreement with the Ciddor model, given it essentially overlaps across all data.

For a better understanding of the differences, we look to the residuals, Figure 12. Here we can see that, in the worst case, residuals are only 0.21 mas. This is a very good agreement and would potentially be adequate for the performance required by MICADO if these results were reflected in reality given the ADC has a residual dispersion budget of 0.4 mas. Note, however, that this would be a significant portion of this budget and so less than ideal.

An important point to mention is that the residuals increase as the dispersion increases. Given we are looking at a limited portion of the wavelength range MICADO will operate in, over the full range of wavelengths we expect the residuals to be worse than 0.21 mas. Therefore, the results here indicate the residuals would grow beyond the ADC budget of 0.4 mas.
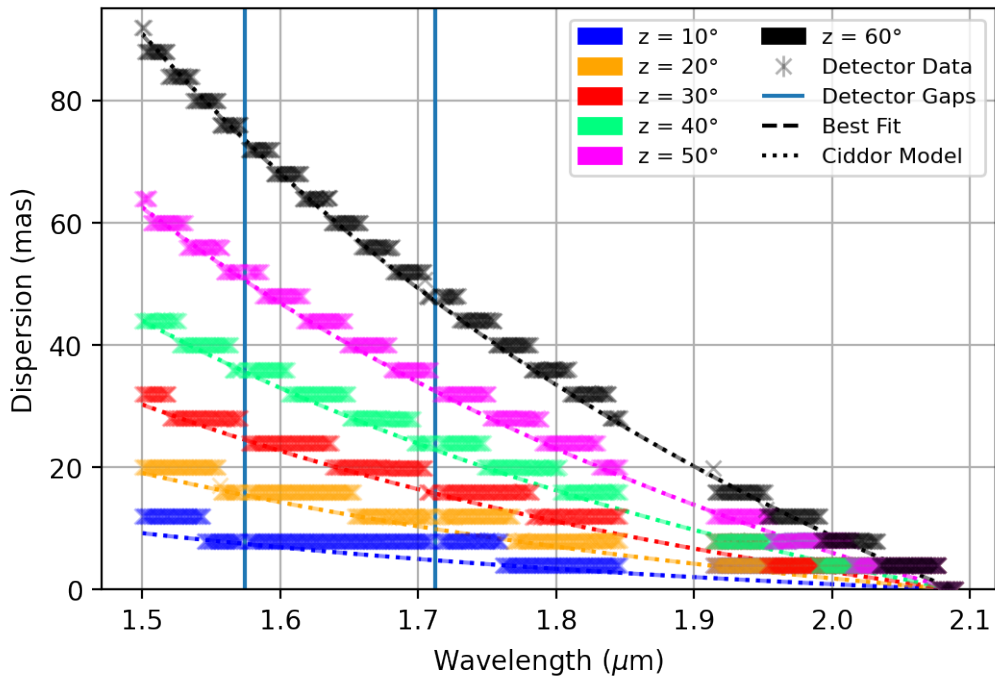
Figure 11: Figure 10 with the Ciddor model overlaid for comparison to our own model. The two models appear to overlap over the whole range of wavelengths analysed on this plot. The residuals in Figure 12 gives a better understanding of the differences.

Figure 12: Residuals of the dispersion comparison between our best fit for the refractive index to that of the Ciddor model. We can see that the residuals increase as dispersion increases. This makes sense since differences between the models will be amplified by larger dispersion.

5.4   Comparison to the Mathar Model

We also overlay the dispersion predicted by the refractive index model of Mathar with our model. This can be seen in Figure 13. While this looks similar to Figure 11 with the Ciddor model, at larger zenith angles a separation between our model and the Mathar model becomes visible. This indicates the residuals should be higher between these models.
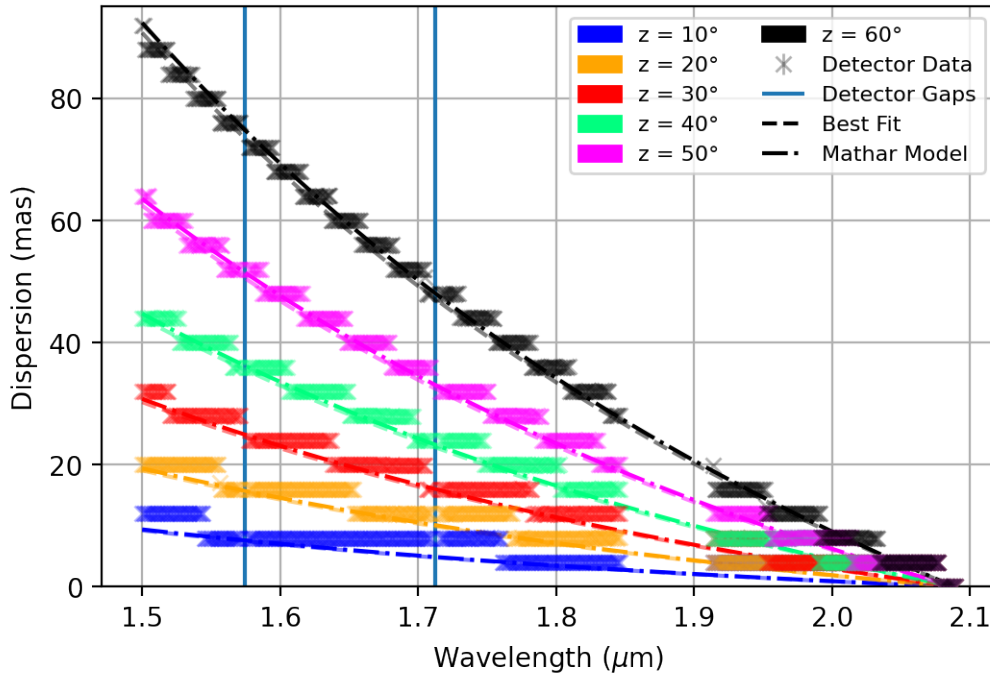

Figure 13: The Mathar model overlaid on Figure 10. Here, small differences between our model and the Mathar model are visible at the largest zenith angles on close inspection. A clearer picture is given by the residuals in Figure 14.

Plotting the residuals proves this to be true. Figure 14 shows the residuals between the Mathar model and ours. At lower zenith angles residuals are already significant and these become larger than 1 mas for the largest zenith angles. If these residuals were present in reality, we would expect some dispersion still present in the image even using the ADC. These residuals exceed the residual dispersion budget of the ADC at most zenith angles. This would be inadequate for the optimal operation of MICADO and, as stated for the Ciddor comparison, would continue to get worse as the wavelength range is increased.

5.5   Refractive Index

In order to find the Cauchy Coefficients for our refractive index model, a linear least-squares fit is done on all the dispersion data for all the zenith angles, once again using `curve_fit`. Since the index of refraction is not dependent on the zenith angle, all 12 sets of data can be used to obtain a single set of coefficients. This then provides our own model for the refractive index of air for our specific parameters and wavelength range. The atmospheric parameters used can be seen in Appendix A.

Dispersion is measured as the difference in refraction between the wavelength of interest and a
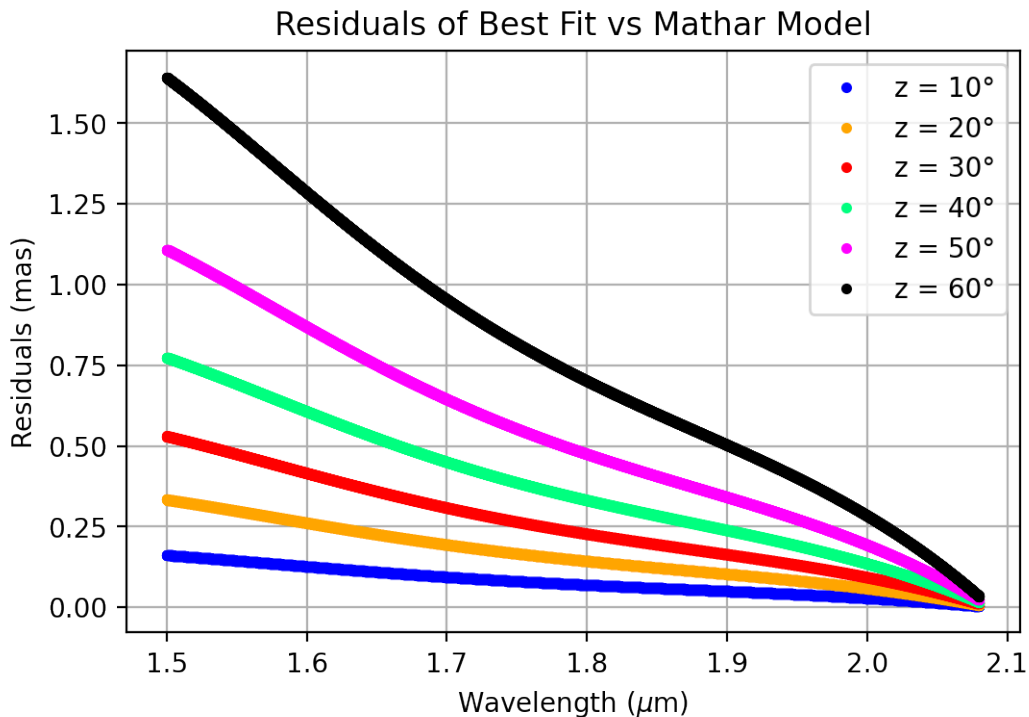
Figure 14: The residuals of the dispersion between our model and that of Mathar. These are significantly larger than the residuals with the Ciddor model, reaching a maximum of 1.64 mas.

reference wavelength. This means, when fitting for our A and B coefficients, we need to fix the refractive index for our reference wavelength or else the A coefficient will cancel and we can only fit for the B coefficient. To obtain a reference refractive index for our fit, the Ciddor model was used due to its expected accuracy over a wide range of different atmospheric conditions.

Once we have our model for the refractive index, we can also directly compare it to other refractive index models. We have done comparisons with the Ciddor (1996) and Mathar (2007) models. This can be seen in Figure 15. We can see that our model is in good agreement with both models, lying between them in the chosen wavelength range. The residuals also reflect this, as we see differences on the order of 10^{-9}, comparable results to that of Spanò (2014).

Such small differences in refractive index lead to very small differences in dispersion as well, as seen in Figure 12 and Figure 14. However, even these small differences are enough to cause dispersion values calculated from different models to deviate from each other at significant levels for MICADO and potentially other instruments designed for ELTs. Refractive index models will need to be reassessed to ensure they are accurate enough for the operation of ELTs as this does not appear to be the case at present.

Comparison of Refractive Index Models
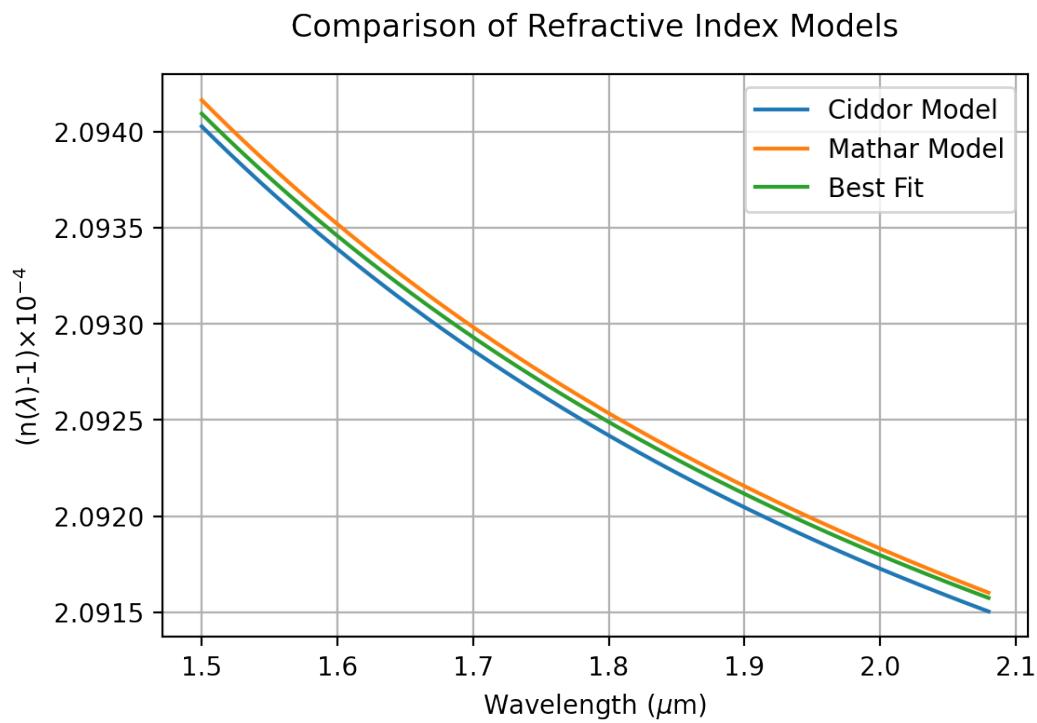
Figure 15: A comparison of our refractive index model with that of Ciddor and Mathar for the same atmospheric conditions. Our model lies between the other two in our wavelength range of interest.

Residuals of Refractive Index Models
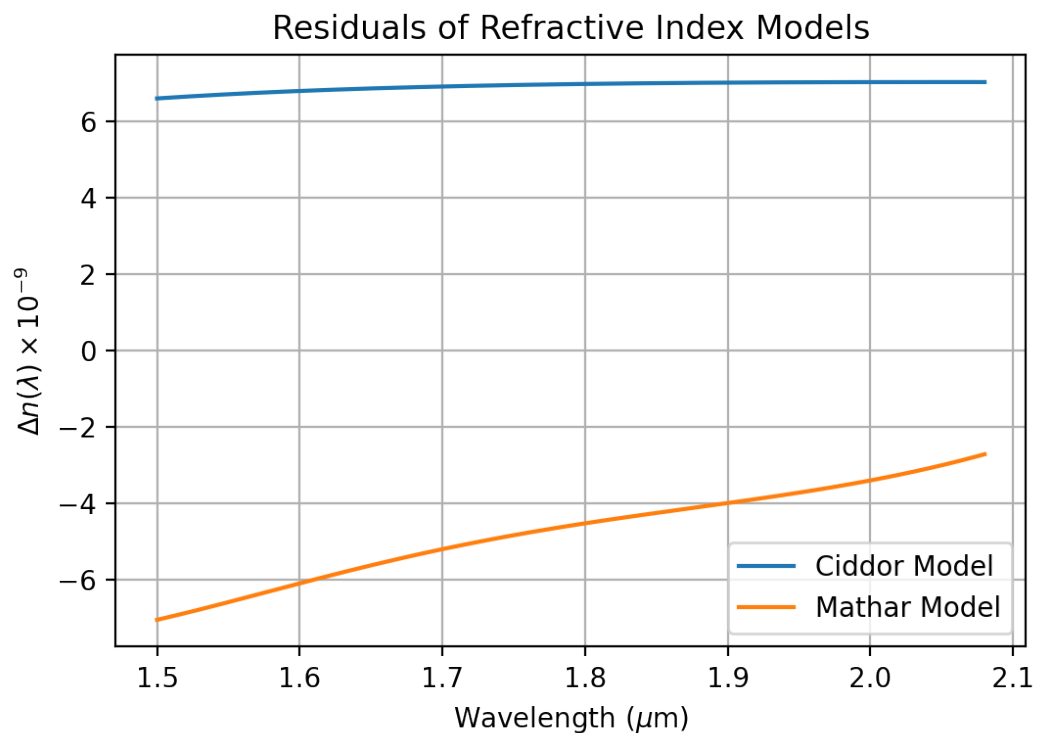
Figure 16: Residuals of our best fit for the refractive index compared to the Ciddor and Mathar models. The differences are below 10^{-8}, similar to results obtained by Spanò (2014).

6 Discussion

We have shown that dispersion could be measured with MICADO in order to compare models to on-sky observations. Performing these observations in reality, once the ELT is complete, would provide further comparison of models to on-sky dispersion as well as potentially offering data that could improve the performance of the ADC by having empirical data taken at the location it will function.

Given that our data suggests current models are not in good enough agreement for the desired performance, measuring dispersion directly with MICADO may be necessary for the desired performance of the ADC to be attained.

Future analysis of dispersion in the context of MICADO would benefit from considering more complex atmospheric models. This would provide a more accurate comparison to reality and more closely resemble the algorithm that the ADC in MICADO will use to compute dispersion. However, for comparing refractive index models to each other, this is unnecessary if all dispersion calculations are using the same geometric model.

6.1 Improved Analysis of Simulations

One might consider several ways to improve the analysis presented here. One such way is to use the spectroscopy IJ filter instead of the HK filter. For our analysis, the simpler trace given by the HK filter allows easier data extraction from the image data. Given that this research was done to assess the feasibility of using ScopeSIM for such analyses, the simpler HK filter was preferred. However, in the IJ bands, dispersion is larger due to the shorter wavelengths, making the measured magnitude of the dispersion more pronounced. This would increase the number of steps in the data seen in Figure 10 and provide for better data at all zenith angles for the model of the refractive index. Additionally, having simulated data on a wider range of wavelengths is important for a complete picture of the effect of dispersion.

Another way the results could be improved is by including multiple point sources across the slit. Analysing the shift in the peaks from all the sources would also reduce the stepped nature of the dispersion data. For certain wavelengths, one or more sources may shift where others do not, depending on their spatial positions on the detector. This would give an indication of sub-pixel dispersion that is not directly simulated by ScopeSIM and was not detectable with a single source.

7 Conclusion

With the ever increasing size of modern telescopes, the effect of atmopsheric dispersion needs to be reconsidered. The ELT is one of the next generation ELTs being built and MICADO will be a first generation instrument that works with the ELT to provide diffraction limited imaging capabilities in the near-infrared. This also means that dispersion will be especially significant for MICADO and could impact the image quality. While MICADO will use an ADC to correct dispersion, it will calculate the needed correction based on a model. Differences between modern models are small but we have shown they can be significant in the context of MICADO.

Atmospheric dispersion can be measured directly using observations made by MICADO in spectroscopy mode, as demonstrated by us using ScopeSIM. These measurements can be compared to existing models to demonstrate differences between real world dispersion and said models. We also demonstrate that ScopeSIM can be used to gain an understanding of how effects like dispersion will affect observations.

From our data analysis and comparison to the Ciddor model, differences in dispersion of up to 0.21 mas are present for our chosen wavelength range, a generally small difference for the intended precision of MICADO and ELTs as a whole but also not the maximum residuals we would expect over MICADO's complete wavelength range. Our comparison to the Mathar model shows that the differences between models can be significant. With differences in the calculated dispersion of up to 1.64 mas, this suggests that differences between current models would impact the operation of MICADO and the ELT and that more specialised models, e.g. optimised for the ELT specifically, are needed for the ADC to perform at the desired level.

Our refractive index model is in good agreement with those of Ciddor and Mathar but this exemplifies why accurate refractive index models are so important for ELTs. Despite their good agreement, with differences of less than 10^{-8}, a measureable difference in the amount of dispersion is still present between our model, Ciddor's, and Mathar's.

The method outlined here is applicable to any telescope implemented by ScopeSIM. It gives a preliminary idea of the dispersion that should be expected and how this will affect observations. So long as the limitations of ScopeSIM are well understood, it is useful to inform a user of the expected performance they might get from a given instrument or telescope. Incorporating a larger range of wavelengths where dispersion is more pronounced and using multiple sources to try and calculate sub-pixel dispersion, more accurate results can be obtained from our method in future analyses.

8 References

Abbott, M. J., Boyd, W. T., Jelinsky, P., Christian, C., Miller-Bagwell, A., Lampton, M., . . .
    Vallerga, J. V. (1996, 11). The Calibration of the EUVE Spectrometers. I. Wavelength
    Calibration and Resolution. *The Astrophysical Journal Supplement Series*, *107*, 451. doi:
    10.1086/192371

Bahrami, M., & Goncharov, A. V. (2011, 08). The achromatic design of an atmospheric
    dispersion corrector for extremely large telescopes. *Optics Express*, *19*, 17099. doi: 10
    .1364/oe.19.017099

Baranne, A., Queloz, D., Mayor, M., Adrianzyk, G., Knispel, G., Kohler, D., . . . Vin, A. (1996,
    10). Elodie: A spectrograph for accurate radial velocity measurements. *Astronomy and
    Astrophysics Supplement Series*, *119*, 373–390. doi: 10.1051/aas:1996251

Beuzit, J.-L., Vigan, A., Mouillet, D., Dohlen, K., Gratton, R., Boccaletti, A., . . . Zurlo, A.
    (2019, 11). SPHERE: the exoplanet imager for the Very Large Telescope. *Astronomy &
    Astrophysics*, *631*, A155. doi: 10.1051/0004-6361/201935251

Birkmann, S. M., Böker, T., Ferruit, P., Giardino, G., Jakobsen, P., de Marchi, G., . . . Brockley-
    Blatt, C. (2011, 09). Wavelength calibration of the JWST near-infrared spectrograph
    (NIRSpec). *SPIE Proceedings*. doi: 10.1117/12.893896

Brandl, B., Bettonvil, F., van Boekel, R., Glauser, A., Quanz, S., Absil, O., . . . the METIS
    Consortium (2021, 03). METIS: The Mid-infrared ELT Imager and Spectrograph . *The
    Messenger*, *182*, 22-26. doi: 10.18727/0722-6691/5218

Ciddor, P. E. (1996, Mar). Refractive index of air: new equations for the visible and near
    infrared. *Appl. Opt.*, *35*(9), 1566–1573. doi: 10.1364/AO.35.001566

Ciliegi, P., Agapito, G., Aliverti, M., Arcidiacono, C., Balestra, A., Baruffolo, A., . . . Zoltan,
    H. (2020, 12). MAORY: the adaptive optics module for the Extremely Large Telescope
    (ELT). *Adaptive Optics Systems VII*. doi: 10.1117/12.2561754

Davies, R., Barl, L., Baudoz, P., Bender, R., Bizenberger, P., Buey, T., . . . Wagner, R. (2018,
    07). The MICADO first light imager for the ELT: overview, operation, simulation. *Ground-
    based and Airborne Instrumentation for Astronomy VII*. doi: 10.1117/12.2311483

Davies, R., Hörmann, V., Rabien, S., Sturm, E., Alves, J., Clénet, Y., . . . The MICADO
    Consortium (2021, 03). Micado: The multi-adaptive optics camera for deep observations.
    The Messenger, *182*, 17-21. doi: 10.18727/0722-6691/5217

Devaney, N., Goncharov, A. V., & Dainty, J. C. (2008, 03). Chromatic effects of the atmosphere
    on astronomical adaptive optics. *Applied Optics*, *47*, 1072. doi: 10.1364/ao.47.001072

Filippenko, A. V. (1982, 08). The importance of atmospheric differential refraction in spec-
    trophotometry. *Publications of the Astronomical Society of the Pacific*, *94*, 715. doi:
    10.1086/131052

Harris, C. R., Millman, K. J., van der Walt, S. J., Gommers, R., Virtanen, P., Cournapeau, D.,
    . . . Oliphant, T. E. (2020). Array programming with NumPy. *Nature*, *585*, 357–362. doi:
    10.1038/s41586-020-2649-2

Labiano, A., Argyriou, I., Álvarez Márquez, J., Glasse, A., Glauser, A., Patapis, P., . . . Van-
    denbussche, B. (2021, 12). Wavelength calibration and resolving power of the JWST
    MIRI Medium Resolution Spectrometer. *Astronomy & Astrophysics*, *656*, A57. doi:
    10.1051/0004-6361/202140614

Leschinski, K., Buddelmeijer, H., Czoske, O., Verdugo, M., Verdoes-Kleijn, G., & Zeilinger,
    W. W. (2020, 12). ScopeSim: a flexible general purpose astronomical instrument data
    simulation framework in Python. *Software and Cyberinfrastructure for Astronomy VI*.
    doi: 10.1117/12.2559784

Lim, P. L., & Hanley, C. (2016). Synphot.
    doi: 10.5281/zenodo.3971036

Maire, A.-L., Chauvin, G., Vigan, A., Gratton, R., Langlois, M., Girard, J. H., ... Zurlo, A.
    (2021, 06).   High-precision Astrometric Studies in Direct Imaging with SPHERE.   *The
    Messenger*, *183*, 7-12. doi: 10.18727/0722-6691/5228

Mangum, J. G., & Wallace, P. (2015, 01). Atmospheric refractive electromagnetic wave bending
    and propagation delay. *Publications of the Astronomical Society of the Pacific*, *127*, 74-91.
    doi: 10.1086/679582

Mathar, R. J. (2007, apr). Refractive index of humid air in the infrared: model fits. *Journal of
    Optics A: Pure and Applied Optics*, *9*(5), 470–476. doi: 10.1088/1464-4258/9/5/008

Owens, J. C. (1967, 01). Optical Refractive Index of Air: Dependence on Pressure, Temperature
    and Composition. *Applied Optics*, *6*, 51. doi: 10.1364/ao.6.000051

Pickles, A. J. (1998, 07). A Stellar Spectral Flux Library: 1150–25000 Å. *Publications of the
    Astronomical Society of the Pacific*, *110*, 863-878. doi: 10.1086/316197

Skemer, A. J., Hinz, P. M., Hoffmann, W. F., Close, L. M., Kendrew, S., Mathar, R. J., ...
    Kelley, M. S. (2009, 08). A direct measurement of atmospheric dispersion in¡¿n¡/i¿-band
    spectra: Implications for mid-ir systems on elts1. *Publications of the Astronomical Society
    of the Pacific*, *121*, 897-904. doi: 10.1086/605312

Spanò, P. (2014, 07). Accurate astronomical atmospheric dispersion models in zemax. *Advances
    in Optical and Mechanical Technologies for Telescopes and Instrumentation*. doi: 10.1117/
    12.2057072

Thatte, N., Tecza, M., Schnetler, H., Neichel, B., Melotte, D., Fusco, T., ... Consortium, H.
    (2021, 03).   HARMONI: the ELT's First-Light Near-infrared and Visible Integral Field
    Spectrograph. *The Messenger*, *182*, 7-12. doi: 10.18727/0722-6691/5215

Tull, R. G., MacQueen, P. J., Sneden, C., & Lambert, D. L. (1995, 03). The high-resolution cross-
    dispersed echelle white-pupil spectrometer of the mcdonald observatory 2.7-m telescope.
    Publications of the Astronomical Society of the Pacific, *107*, 251. doi: 10.1086/133548

van den Born, J. A., & Jellema, W. (2020, 06). Quantification of the expected residual dispersion
    of the MICADO Near-IR imaging instrument. *Monthly Notices of the Royal Astronomical
    Society*, *496*, 4266-4275. doi: 10.1093/mnras/staa1870

Vernet, E., Cirasuolo, M., Cayrel, M., Tamai, R., Kellerer, A., Pettazzi, L., ... Team, T. E.
    (2019, 12). ELT M4 — The Largest Adaptive Mirror Ever Built. *The Messenger*, *178*,
    3-4. doi: 10.18727/0722-6691/5162

Vernet, E., Pirard, J.-F., Araujo Hauck, C., Zuluaga-Ramírez, P., Cayrel, M., Lamour, C., ...
    Claeyssen, F. (2020, 12). ESO ELT M5 Unit: design and manufacturing status. *Ground-
    based and Airborne Telescopes VIII*. doi: 10.1117/12.2561016

Virtanen, P., Gommers, R., Oliphant, T. E., Haberland, M., Reddy, T., Cournapeau, D., ...
    SciPy 1.0 Contributors (2020). SciPy 1.0: Fundamental Algorithms for Scientific Com-
    puting in Python. *Nature Methods*, *17*, 261–272. doi: 10.1038/s41592-019-0686-2

Wehbe, B., Cabral, A., Martins, J. H. C., Figueira, P., Santos, N. C., & Ávila, G. (2019, 11).
    The impact of atmospheric dispersion in the performance of high-resolution spectrographs.
    Monthly Notices of the Royal Astronomical Society, *491*, 3515-3522. doi: 10.1093/mnras/
    stz3256

Wehbe, B., Cabral, A., & Ávila, G. (2020, 09). On-sky measurements of atmospheric dispersion
    – I. Method validation. *Monthly Notices of the Royal Astronomical Society*, *499*, 183-192.
    doi: 10.1093/mnras/staa2726

Wynne, C. G., & Worswick, S. P. (1986, 06). Atmospheric dispersion correctors at the cassegrain
    focus. *Monthly Notices of the Royal Astronomical Society*, *220*, 657-670. doi: 10.1093/

mnras/220.3.657

Young, A. T. (2006, 04). Understanding astronomical refraction. *The Observatory*, *126*, 82-115.

A   Atmospheric Conditions

Parameter	Value
Temperature	280.15°K (7°C)
Pressure	75.5 kPa
Humidity	10%
CO_2 Content	370 ppm

Table 1: Atmospheric conditions used to compute dispersion. These values are used by ScopeSIM and the AstroAtmosphere package. While CO_2 content is typically considered 450 ppm, the Mathar model was based on a content of 370 ppm so for our comparison this value was also chosen.
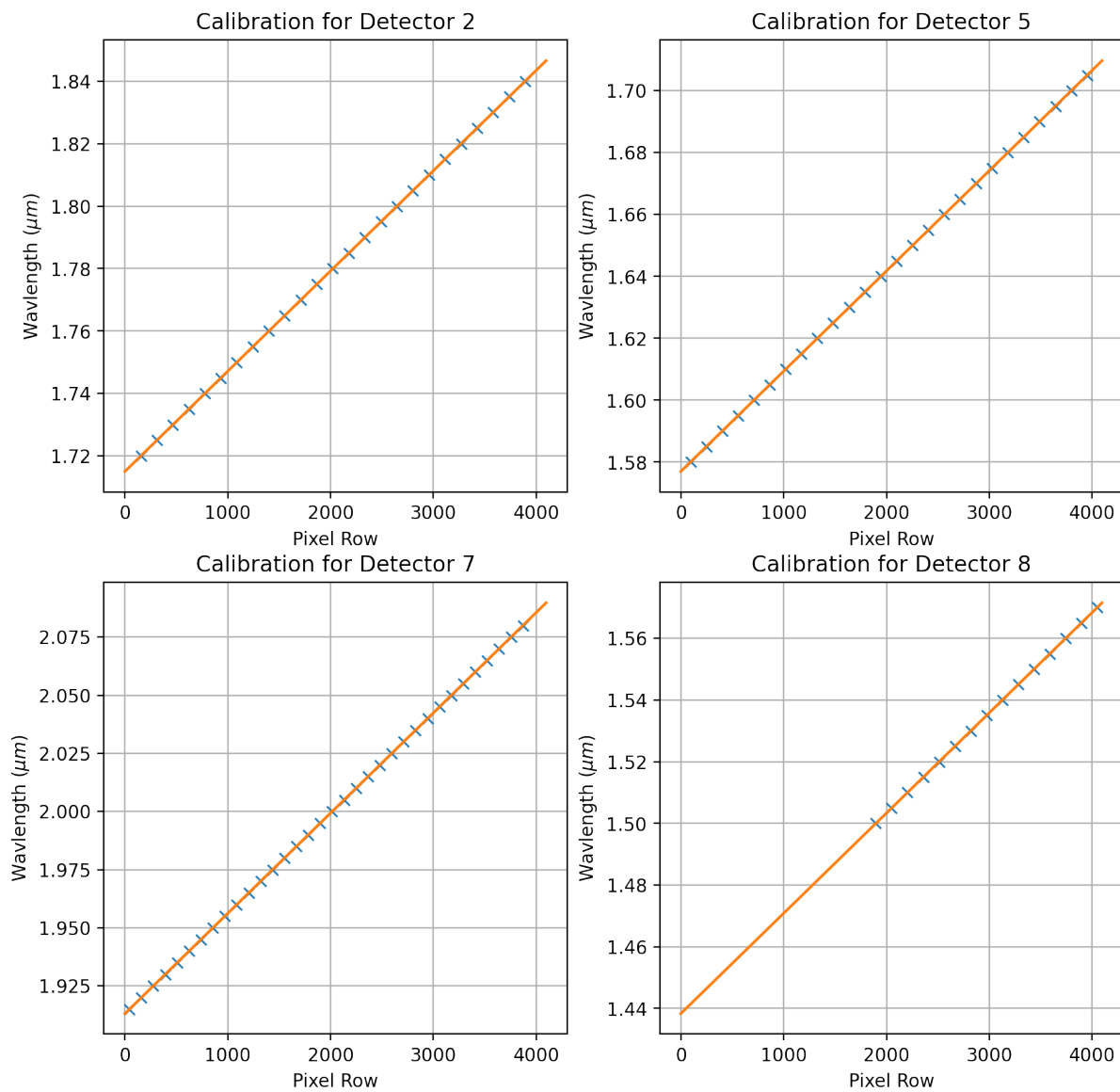
B   Calibration Results

The results from the calibration allowed us to relate a given pixel row to its corresponding wavelength for our trace analysis. These results are given here. The relation between pixel row and wavelength appeared linear across all four detectors that were looked at. However, the relation itself was not the same for all detectors looked at. Detector 7 in particular had a much steeper relation and therefore contained a larger range of wavelengths.

A simple straight line was fitted to each detectors data set using a linear least squares function, in this case NumPy's polyfit (Harris et al., 2020). This gave the wavelength on the bottom pixel row and the step in wavelength per pixel row. These values are outlined in Table 2. These fits were plotted over the calibration peaks from the detectors as a sanity check. These plots can be seen in Figure 17. These plots confirmed that the relation was indeed linear for each detector. Since the spectral trace does not extend over the entirety of detector 8, fewer calibration peaks could be included. However, this was still sufficient for our purposes.

| Detector	Slope ($\times 10^{-5}$)	Intercept
2	3.2101 ± 0.0009	1.71506 ± 0.00002
5	3.2400 ± 0.0005	1.57698 ± 0.00001
7	4.3116 ± 0.0002	1.91310 ± 0.00005
8	3.2511 ± 0.0004	1.43834 ± 0.00001

Table 2: The calibration parameters used to match a wavelength to a pixel row or vice versa.

Figure 17: Calibration data and its best fit. We can see that the calibration data is linear across all detectors but that the slope in the best fit varies.

C   Individual Dispersion Results

To improve readability, only part of the the complete dataset was shown in our results. Here we present our measured dispersion data, along with the best fit model and Ciddor model overlaid, for each zenith angle separatley.
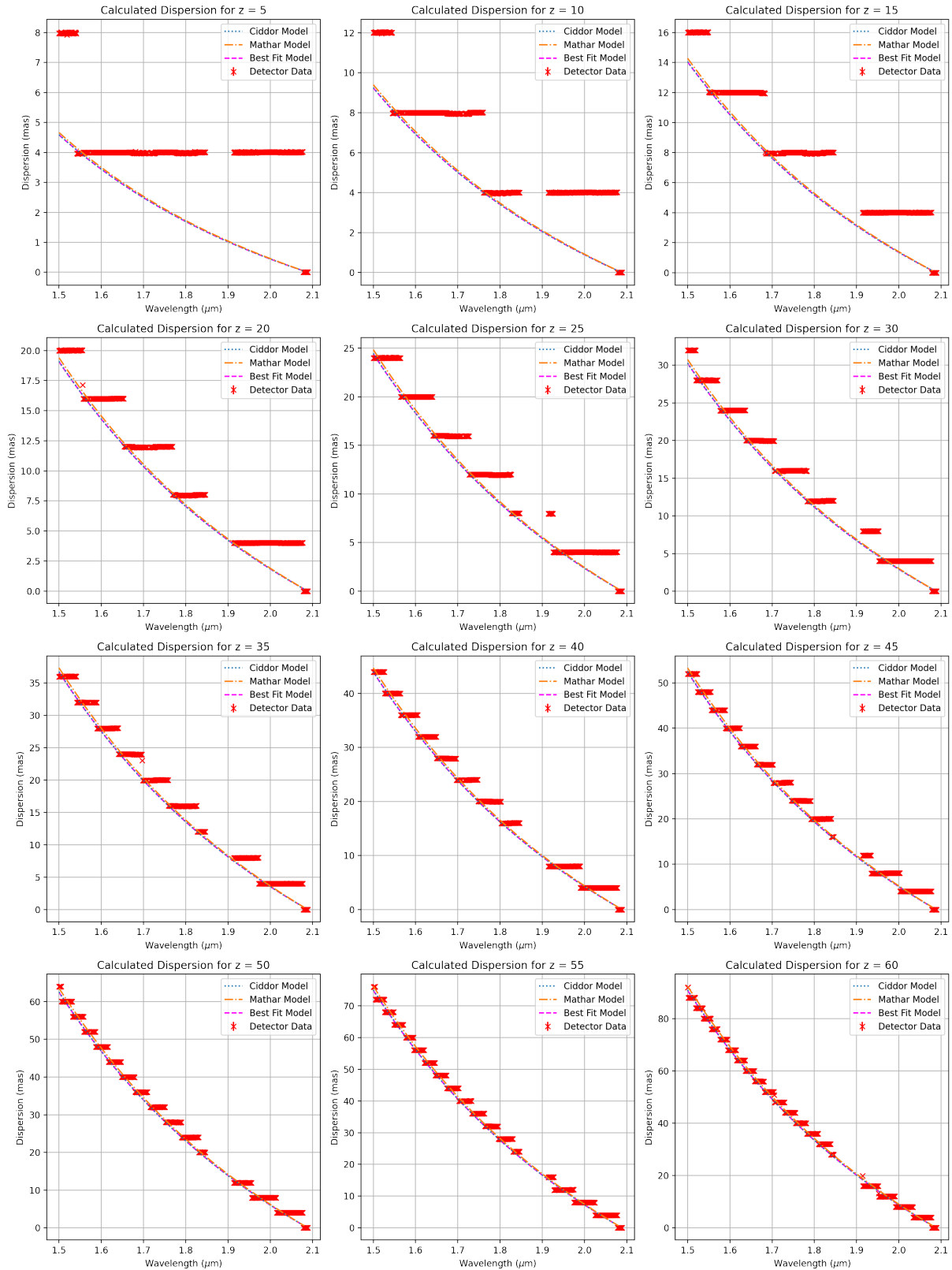
Figure 18: Our dispersion data at each zenith angle presented individually. All data was used for our model and calculations. Our model and the Ciddor model have also been included for each zenith angle.